

Epitaxial Er-doped Y_2O_3 on silicon for quantum coherent devices

Cite as: APL Mater. **8**, 031111 (2020); <https://doi.org/10.1063/1.5142611>

Submitted: 15 December 2019 . Accepted: 26 February 2020 . Published Online: 13 March 2020

Manish Kumar Singh , Abhinav Prakash , Gary Wolfowicz , Jianguo Wen , Yizhong Huang, Tijana Rajh , David D. Awschalom , Tian Zhong , and Supratik Guha 



View Online



Export Citation



CrossMark

ARTICLES YOU MAY BE INTERESTED IN

[Developing silicon carbide for quantum spintronics](#)


Applied Physics Letters **116**, 190501 (2020); <https://doi.org/10.1063/5.0004454>

[Stark tuning and electrical charge state control of single divacancies in silicon carbide](#)

Applied Physics Letters **111**, 262403 (2017); <https://doi.org/10.1063/1.5004174>

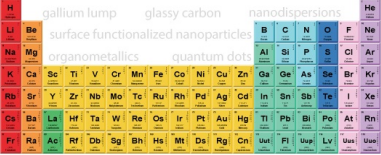
[Heterodyne detection of radio-frequency electric fields using point defects in silicon carbide](#)

Applied Physics Letters **115**, 043105 (2019); <https://doi.org/10.1063/1.5108913>



AMERICAN ELEMENTS

THE ADVANCED MATERIALS MANUFACTURER®



additive manufacturing epitaxial crystal growth cerium oxide polishing powder silver nanoparticles sputtering targets III-IV semiconductors CVD precursors europium phosphors

deposition slugs OLED Lighting spintronics solar energy osmium nanoribbons thin films chalcogenides AuNPs GDC Li-ion battery electrolytes 99.999% ruthenium spheres

endohedral fullerenes copper nanoparticles diamond micropowder CIGS MBE grade materials palladium catalysts flexible electronics beta-barium borate borosilicate glass dysprosium pellets YBCO pyrolytic graphite 3d graphene foam indium tin oxide mesoporous silica raman substrates sapphire windows tungsten carbide InGaAs barium fluoride carbon nanotubes lithium niobate scandium powder

gallium lump glassy carbon nanodispersions InAs wafers laser crystals ultra high purity materials MOFs rare earth metals photovoltaics refractory metals MOCVD superconductors transparent ceramics ultra high purity silicon

American Elements opens up a world of possibilities so you can **Now Invent!**

Over 15,000 certified high purity laboratory chemicals, metals, & advanced materials and a state-of-the-art Research Center. Printable GHS-compliant Safety Data Sheets. Thousands of new products. And much more. All on a secure multi-language "Mobile Responsive" platform.

perovskite crystals yttrium iron garnet alternative energy h-BN gold nanocubes graphene oxide macromolecules photonics rhodium sponge fiber optics beamsplitters infrared dyes zeolites fused quartz metallocenes platinum ink buckyballs Ti-6Al-4V

Now Invent.™

The Next Generation of Material Science Catalogs

www.americanelements.com



Epitaxial Er-doped Y_2O_3 on silicon for quantum coherent devices

Cite as: APL Mater. 8, 031111 (2020); doi: 10.1063/1.5142611

Submitted: 15 December 2019 • Accepted: 26 February 2020 •

Published Online: 13 March 2020



Manish Kumar Singh,¹ Abhinav Prakash,^{1,2} Gary Wolfowicz,^{1,2} Jianguo Wen,² Yizhong Huang,¹ Tijana Rajh,^{2,a)} David D. Awschalom,^{1,2} Tian Zhong,^{1,a)} and Supratik Guha^{1,2,a)}

AFFILIATIONS

¹Pritzker School of Molecular Engineering, University of Chicago, Chicago, Illinois 60637, USA

²Argonne National Laboratory, Lemont, Illinois 60439, USA

^{a)}Authors to whom correspondence should be addressed: rajh@anl.gov; tzh@uchicago.edu; and guha@uchicago.edu

ABSTRACT

Rare-earth ions (REIs) have incomplete $4f$ shells and possess narrow optical intra- $4f$ transitions due to shielding from electrons in the $5s$ and $5p$ orbitals, making them good candidates for solid-state optical quantum memory. The emission of Er^{3+} in the telecom C-band (1530 nm–1565 nm) makes it especially attractive for this application. In order to build practical, scalable devices, the REI needs to be embedded in a non-interacting host material, preferably one that can be integrated with silicon. In this paper, we show that Er^{3+} can be isovalently incorporated into epitaxial Y_2O_3 thin films on Si (111). We report on the synthesis of epitaxial, single-crystalline $\text{Er}:\text{Y}_2\text{O}_3$ on Si with a narrow inhomogeneous linewidth in the photoluminescence (PL) spectra, 5.1 GHz (<100 mK), and an optical excited state lifetime of 8.1 ms. The choice of Y_2O_3 was driven by its low nuclear spin and small lattice mismatch with Si. Using PL and electron paramagnetic resonance, we show that Er^{3+} substitutes for Y in the crystal lattice. The role of interfacial SiO_x , diffusion of silicon into the film, and the effect of buffer layers on the inhomogeneous PL linewidth are examined. We also find that the linewidth decreased monotonically with film thickness but surprisingly exhibits no correlation with the film crystalline quality, as measured by the x-ray rocking curve scans, suggesting other factors at play that limit the inhomogeneous broadening in Y_2O_3 films.

© 2020 Author(s). All article content, except where otherwise noted, is licensed under a Creative Commons Attribution (CC BY) license (<http://creativecommons.org/licenses/by/4.0/>). <https://doi.org/10.1063/1.5142611>

I. INTRODUCTION

The need for quantum memory devices has been increasingly apparent in networked coherent quantum systems that use an optical quantum communication link within a distributed network of processors or a secure communication network that uses quantum repeaters.^{1–3} The role of a quantum memory is to store quantum information during entanglement events, and multiple mechanisms and systems for storage have been identified by researchers.^{4,5} A promising and convenient approach among them is to use the spin-optical interfaces of rare-earth ions (REIs).^{6–10} Rare-earth ions have full $5s$ and $5p$ orbitals that shield the inner $4f$ levels from the local environment, resulting in narrow $4f$ – $4f$ electronic transitions. This shielding results in a low spectral diffusion not achievable in other systems such as the nitrogen-vacancy center defects.⁹ Additionally, they are well suited for the development of coherent microwave to optical transduction.¹¹ These properties make REIs

ideal for solid-state optical quantum memory systems, provided they can be embedded in a sufficiently inert (low nuclear spin and no unpaired electrons) solid-state host material and are capable of being modulated electrically or optically in an efficient manner. Among REIs, Er^{3+} is particularly attractive since it has an optical transition (~ 1535 nm for $^4\text{I}_{13/2} \rightarrow ^4\text{I}_{15/2}$) that lies in the telecom C-band ($\lambda = 1530$ nm–1565 nm), enabling the use of existing in-ground fiber links and leveraging the extremely low transmission loss in this wavelength range (0.2 dB/km).

Properties of active REIs in Y_2O_3 nanoparticles and ceramic hosts have been extensively studied in the past.^{12–19} This includes a reported optical homogeneous linewidth of 85.6 kHz¹⁴ and a spin coherence time of 2.9 ms in $\text{Eu}:\text{Y}_2\text{O}_3$.¹⁹ These studies have been covered in detail in recent reviews.^{20–22} For crystalline host materials, the focus has been on bulk single crystals, such as yttrium orthosilicate (Y_2SiO_5 or YSO), yttrium vanadate (YVO_4 or YVO), and yttrium aluminum garnet ($\text{Y}_3\text{Al}_5\text{O}_{12}$ or YAG). These

studies^{23–27} have demonstrated long coherence times for the hyperfine transitions in these host materials—coherence time is a key metric for the duration that quantum information can be stored in a system. Recent work, using a combination of methods, has demonstrated a hyperfine coherence time of 1.3 s ($T = 1.4$ K, $B = 7$ T) in an Er^{3+} :YSO host²⁶ and over 6 h ($T = 2$ K) for Eu^{3+} .²⁷ Recent studies have also demonstrated that nanophotonic devices can be used to isolate single atoms in these systems. For instance, Dibos *et al.*⁶ explored the fabrication of an evanescently coupled structure out of silicon and stamping onto the bulk. A different approach used focused ion beam milling to create nanobeam structures from the bulk single crystal.²⁸ These demonstrations show the promise of REIs, but they are limited by bulk platforms and fabrication methods that are not scalable. From a device perspective, deployment of REIs for quantum memory needs a convenient and scalable means of interrogating the REI—i.e., *storing* quantum information and *retrieving* it from memory.

One way of accomplishing scalability and compact operability is via the use of Er^{3+} ions embedded in a thin film solid-state host that can be grown and integrated directly onto a silicon platform, enabling potential integration with silicon photonic components and fabrication of low mode volume, high Q-factor compact resonators, and electronics that will enable us to address the hyperfine states. Evaluation of the optical and microstructural properties of Er doped epitaxial rare earth oxide thin films has not been done before. This is the objective of the current research, and in this paper, we explore and evaluate the microstructural, chemical, and optical properties of Er^{3+} in epitaxial Y_2O_3 and $(\text{La}_x\text{Y}_{1-x})_2\text{O}_3$ oxide heterostructures on Si wafers for their suitability in scalable quantum memories. The host material is preferred to be single-crystalline to minimize heterogeneous variations in the environment surrounding the embedded REI ions that are expected to induce additional spin-lattice and spin-spin relaxation pathways and reduce the optical and spin coherence times. There are a few considerations that govern the selection of a good host material for optically active REIs:

- (i) A cubic host is preferable with low lattice mismatch between the host material and silicon for high-quality epitaxial growth and silicon integration.
- (ii) Low or zero nuclear and electron spin is preferred in the host material.
- (iii) Isovalent incorporation of the REI ion at a substitutional site.
- (iv) Low optical loss or absorption in the telecom band.

When considering Er^{3+} , several rare-earth sesquioxides satisfy criteria (i) and (iii) (small lattice mismatch and isovalence). Among these, the lowest nuclear spin is offered by Y_2O_3 , Gd_2O_3 , and Tb_2O_3 with nuclear spins of 1/2, (0, 3/2), and (0, 3/2) respectively, along with lattice mismatches of -2.4% , -0.48% , and -1.22% . Among these, Y possesses no unpaired electrons, which could be a source of magnetic noise. Furthermore, the ionic radii of Y^{3+} and Er^{3+} are similar (Shannon radius of 102 pm and 103 pm, respectively), and therefore, local strain effects are expected to be minimal. Additionally, as yttrium has only one stable isotope with $\frac{1}{2}$ nuclear spin, it provides a *uniform* distribution of nuclear spins around Er^{3+} ions. These properties make Y_2O_3 an attractive host material for erbium.

While the growth of epitaxial $\text{Y}_2\text{O}_3/\text{Si}$ structures has been studied before using both Molecular Beam Epitaxy (MBE)^{29,30}

and pulsed laser deposition (PLD) techniques,^{31,32} Er-doped Y_2O_3 ($\text{Er}:\text{Y}_2\text{O}_3$) and the evaluation of such heterostructures for quantum memory and related devices remain unexplored. In this paper, we demonstrate the successful epitaxial growth of $\text{Er}:\text{Y}_2\text{O}_3$ on Si (111) substrates and carry out a detailed microstructural and optical characterization study of these films. Through careful optimization of the growth conditions, we show that narrow photoluminescence (PL) inhomogeneous linewidths (7.9 GHz at 4 K) for the first optical transition of Er^{3+} can be obtained, indicating that Y_2O_3 epitaxial films can act as an inert, high quality host for Er^{3+} . The hyperfine levels from the 7/2 nuclear spin isotope ^{167}Er can be seen clearly in the Electron Paramagnetic Resonance (EPR) spectrum. We show that the catalytic interfacial oxidation of the Si/ Y_2O_3 interface, the diffusion of silicon into the oxide layer, and possible diffusion/contamination effects from surfaces are key material phenomena that need to be controlled and demonstrate how a buffer layer approach can mitigate these effects. No significant correlation between the Er^{3+} PL linewidths and the crystal quality, as determined by x-ray rocking curves, was observed, indicating that structural distortions due to mosaicity and dislocations in the film may not play a significant role for quantum device development in such heterostructures. On the other hand, we observe a clear inverse correlation between the PL linewidth and the film thickness, lending further support to the potential role of the proximity of surfaces and interfaces. Finally, we show that alloying this system (Y_2O_3) with a high quantity of lanthanum, which leads to a closer lattice matching condition,²⁹ also results in broadening of the PL linewidth.

II. METHODS

A. Growth of epitaxial thin films

Epitaxial growths of Y_2O_3 thin films were performed on Si (111) substrates in a Riber oxide MBE system with a background pressure of $\sim 10^{-10}$ Torr. Substrates were prepared using a piranha clean followed by a dilute hydrofluoric acid (HF) dip. The epitaxial growth was initiated on 7×7 reconstructed Si (111) surfaces. A range of substrate temperatures between 600°C and 920°C was explored for the growth. High purity (4 N in total metal basis and 5 N in rare earth metal basis)³³ erbium, lanthanum, and yttrium were evaporated using high-temperature effusion cells, and an RF plasma source was used for oxygen (325 W, 2.8 sccm) corresponding to a pressure of $\sim 2 \times 10^{-5}$ Torr in the growth chamber. Er concentrations between 10 ppm and 200 ppm were used for different samples by varying the Er cell temperature between 700°C and 900°C , respectively. A higher concentration was needed to get a good PL intensity during measurements. We compared the inhomogeneous linewidth for concentrations in this range (10 ppm, 50 ppm, and 200 ppm) and did not find any significant differences. The Er concentration was estimated using an Er_2O_3 film grown with an Er cell temperature of 1200°C and extrapolating the vapor pressure³⁴ to lower cell temperatures. The epitaxial growth was monitored *in situ* by reflection high-energy electron diffraction (RHEED).

B. Film characterization

Y_2O_3 ($a = 10.60$ Å, space group $\text{Ia}\bar{3}$, and $Z = 16$) has a bixbyite structure with 32 cation (Y^{3+}) sites out of which 24 are non-centrosymmetric C_2 sites and 8 are centrosymmetric C_{3i} sites.³⁵ Out

of these, there are 6 magnetically inequivalent for C_2 and 4 for C_{3i} . Given the similar ionic radii, Er^{3+} is expected to substitute for Y^{3+} at both sites during growth.

Ex situ structural characterization was performed using a high-resolution x-ray diffractometer (Bruker D8 Discover). Optical characterization was realized in a confocal microscopy setup. Off-resonant optical spectra were obtained following excitation with a 976 nm laser, and the emission was detected using a nitrogen-cooled InGaAs camera. Resonant optical spectra for the transition at ~ 1535 nm were realized using a tunable C-band laser (ID photonics CoBrite DX1) with the PL detected using a single nanowire single photon detector (SNSPD, Quantum Opus). In this case, the excitation and the PL signal were temporally isolated from each other using a combination of optical switches and acousto-optic modulators. The samples were mounted on a copper cold-finger in a closed-cycle cryostat (Montana Instruments). All reported measurements in this setup were performed at 4 K unless otherwise noted in the text.

A dilution fridge setup was used for the mK measurement, and a schematic is provided in the [supplementary material](#). The sample was mounted on a three-axis nano-positioner via a copper plate. The laser pulses (Toptica CTL1500) were generated by two tandem acousto-optic modulators (AOMs) with ~ 100 dB on/off ratio. The pulse sequence with 15 ms pulse width and 10 Hz repetition rate was focused with an aspheric lens pair. The reflected light was collected and delivered to a superconducting nanowire detector (SNSPD) on the cold plate in the same fridge. An optical switch inserted in front of the SNSPD blocks the strong excitation pulse and transmits the emitted light.

X-band EPR was conducted using a Bruker Elexsys E500 system equipped with a variable-temperature cryostat (Oxford). The measurements were performed in a flow cryostat at 4.2 K. The g -factors were calibrated for homogeneity and accuracy by comparing to the Mn^{2+} standard in a SrO matrix ($g = 2.0012 + 0.0002$)³⁶ and by using coal samples with $g = 2.00285 \pm 0.00005$,³⁷ respectively.

High-resolution transmission electron microscopy (HRTEM) was carried out using the Argonne Chromatic Aberration-corrected TEM (ACAT, FEI Titan 80-300ST TEM/STEM) with a field-emission gun and an image corrector to correct both spherical and chromatic aberrations, enabling a resolution limit better than 0.8 Å at an accelerating voltage of 200 kV. High-angle annular dark-field imaging and energy-dispersive x-ray spectroscopy mapping were carried out using a Talos F200X S/TEM (operating at an accelerating voltage of 200 kV) equipped with an X-FEG gun and a Super-X energy dispersive spectroscopy (EDS) system.

III. RESULTS AND DISCUSSION

A. Film structure

Figure 1(c) shows the wide-angle (2θ - ω) x-ray diffraction pattern for a 180 nm film [~ 140 nm $Er:Y_2O_3$ with 10 ppm Er and with a top cap and bottom buffer, each of ~ 20 nm undoped Y_2O_3 , as shown in the schematic Fig. 1(a)] grown on the Si (111) substrate at 850 °C, showing $Y_2O_3(222)/Si(111)$ and $Y_2O_3[0\bar{1}1]/Si[110]$ epitaxial relationship. The presence of finite-size thickness (Pendellösung) fringes and a streaky RHEED pattern [Fig. 1(b)] suggests a smooth and crystalline film.

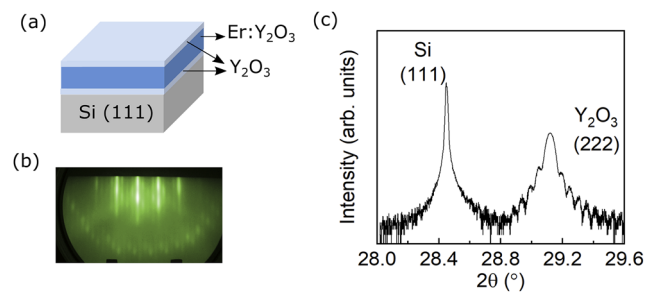


FIG. 1. (a) Schematic of the film for which the data are shown, (b) the streaky RHEED pattern following the end of growth, indicating a smooth and crystalline film, and (c) XRD pattern showing the Si (111) substrate and Y_2O_3 (222) film peaks.

The crystalline and epitaxial nature of film growth was further studied using transmission electron microscopy (TEM). Figure 2(a) shows a cross section transmission electron micrograph of the 460 nm Y_2O_3 film grown on Si (111) along with a high-resolution TEM image and a selected area electron diffraction image (inset) of the film consistent with the bixbyite structure of Y_2O_3 .

B. Engineering the film-interfaces

The high-resolution TEM image of the film/substrate interface and the energy dispersive spectroscopy (Fig. 3) indicates two amorphous layers, one of which is caused by Si oxidation at the Si interface. This SiO_x layer transitions to a phase consisting of Y, Si, and O that is proximal to the Y_2O_3 film. This transition is due to the catalytic behavior of rare-earth oxide overlayers, which results in silicon oxidation.³⁸ The interfacial oxidation occurs after epitaxial growth of Y_2O_3 via the diffusion of reactive oxygen through the film either during growth or *ex situ*. This oxidation can be minimized by reducing the post-growth exposure to oxygen.³⁹

We investigated the effect of growth time and temperature on the presence of interfacial oxides and found that the thickness of the amorphous oxide interface increases with an increase in the growth time and substrate temperature. Figures 3(a)–3(d) show the cross-sectional TEM image, and Figs. 3(e) and 3(f) show the EDS line scans across the interface for two samples grown at 920 °C and 790 °C for 80-min and 60-min long growths, respectively. As seen in the scan, the interfacial oxidation leads to the formation of a silicon diffusion tail into the Y_2O_3 layer. The width of the silicon contaminated zone in Y_2O_3 reduces with a decrease in the growth temperature from 920 °C to 790 °C.

In order to further probe the effect of possible silicon diffusion in the film and to examine the role of surface defects on the optical properties of Er^{3+} , we studied the photoluminescence for three samples with different structures—400 nm $Er:Y_2O_3/Si$ [Figs. 4(a) and 4(d)], 400 nm $Er:Y_2O_3/100$ nm Y_2O_3/Si [Figs. 4(b) and 4(e)], and 200 nm $Y_2O_3/400$ nm $Er:Y_2O_3/100$ nm Y_2O_3/Si [Figs. 4(c) and 4(f)]. The Er concentration in these films was kept constant at ~ 50 ppm level. The inhomogeneous linewidth (Γ_{inh}) measured from the resonant PL for the first sample was 37.4 GHz [Fig. 4(d)]. Insertion of a 100 nm undoped buffer layer decreased the linewidth to 24.0 GHz [Fig. 4(e)]. This decrease in the PL linewidth is attributed

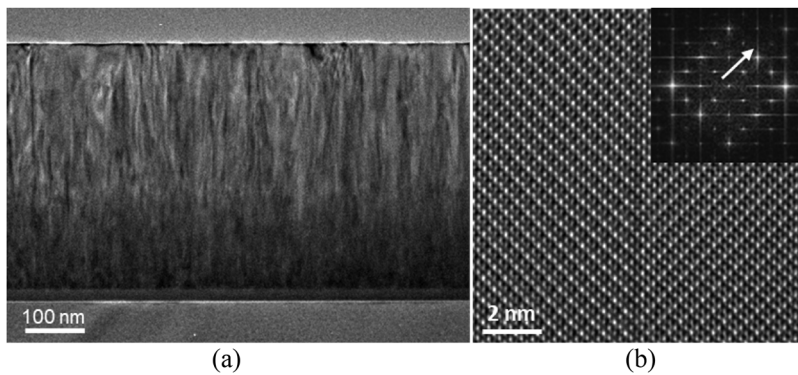


FIG. 2. (a) Cross-sectional TEM of a 460 nm film grown at 920 °C (growth time = 80 min). The interfacial layer is visible. (b) A high-resolution TEM image showing the Y_2O_3 film with a coincidence boundary. The inset shows the diffraction pattern (arrow points in the 400 direction) confirming the bixbyite structure.

to an increased separation between the active Er^{3+} ions from the film/substrate interface. A further decrease in the PL linewidth was observed when the Er^{3+} ions are away from the top interface, the condition shown in Fig. 4(f). The inhomogeneous linewidth for this sample was found to be 19.6 GHz. This *sandwiching* of the optically active $\text{Er}^{3+}:\text{Y}_2\text{O}_3$ layer between undoped Y_2O_3 helped to reduce the inhomogeneous linewidth by about 50%, suggesting that proximity of the interfaces contributes to the broadening seen here. Why does this occur? We believe that the bottom interface and the top surface act as gateways for impurity diffusion into the Y_2O_3 layer. We speculate that these could be trace amounts of Si (from the Si substrate) and/or OH groups and oxygen vacancies (from the top surface exposed to the ambient). Si diffusion is suggested from our EDS scans, and oxygen and OH groups are known to be fast diffusing species^{40,41} in ionic oxides. Such impurities could cause inhomogeneous linewidth broadening of the Er emission via localized charge defect formation from aliovalent substitutional or interstitial accommodation of these impurities or defects in the vicinity of the Er ions.

Due to a lattice mismatch with Si (2.4% tensile), relaxed Y_2O_3 will contain dislocations that relieve the elastic strain. It

has been shown that alloying Y_2O_3 with La can reduce the lattice mismatch with silicon.²⁹ To explore the use of a lattice-matched host material for Er^{3+} , a 80 nm $(\text{La}_x\text{Y}_{1-x})_2\text{O}_3/400$ nm $\text{Er}:(\text{La}_x\text{Y}_{1-x})_2\text{O}_3/20$ nm $(\text{La}_x\text{Y}_{1-x})_2\text{O}_3/\text{Si}$ (111) film was grown with $x = 0, 0.17$, and 0.24 . The Er concentration in these films was kept constant at ~ 200 ppm level. Figures 4(g)–4(i) show a wide-angle x-ray diffraction pattern for the three samples with varying x . Among these samples, the film with $x = 0.17$ had the smallest lattice mismatch (0.37%) with silicon (see the [supplementary material](#) for details of this estimate). Although this film has lower lattice mismatch compared to the unalloyed film (0.37% vs 2.4%), the inhomogeneous linewidth was found to be 7× larger [Figs. 4(j)–4(l)]. This broadening is attributed to the presence of random substitutional disorder in the film due to La substituting at the Y site similar to the results reported for Sc alloyed $\text{Er}:\text{Y}_2\text{O}_3$ ⁴² and $\text{Eu}:\text{Y}_2\text{O}_3$.⁴³ Increasing the amount of La ($x = 0.24$) further increases the inhomogeneous linewidth due to enhanced disorder as well as phase segregation of hexagonal La_2O_3 , as evidenced by an additional diffraction peak in the corresponding 2θ – ω scan. The La fraction was estimated by measuring the ratio of beam equivalent pressures of La and Y (using a beam flux monitor).

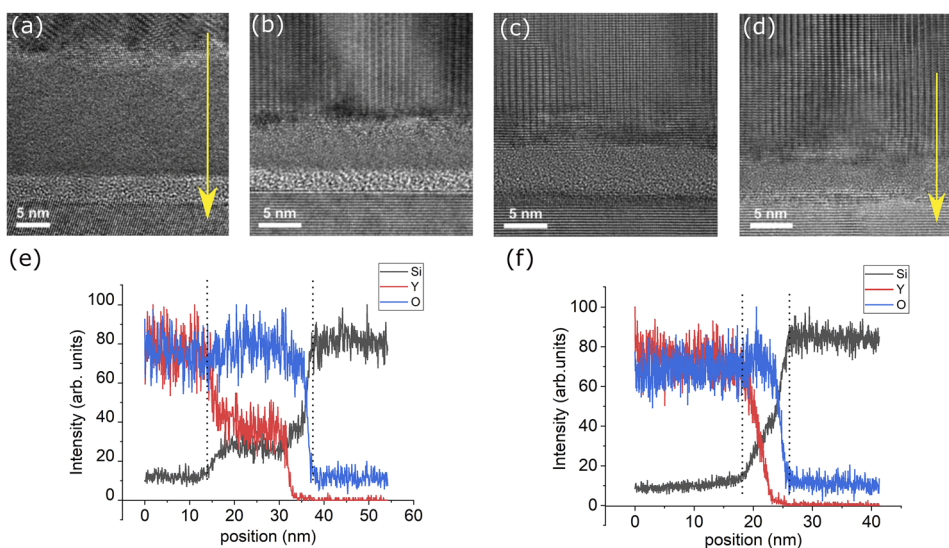


FIG. 3. Cross-sectional TEM showing the interface for four different conditions of temperature (T) and time (t). The thickness of the amorphous layer seen between crystalline Y_2O_3 and SiO_2 can be directly estimated from the TEM (a) 24 nm for $T = 920^\circ\text{C}$, $t = 80$ min, (b) 8 nm for $T = 850^\circ\text{C}$, $t = 80$ min, (c) 5 nm for $T = 790^\circ\text{C}$, $t = 60$ min, and (d) 5 nm for $T = 790^\circ\text{C}$, $t = 180$ min. The EDS of the interface for (a) and (d) is given in figure (e) and (f), respectively. The direction of the EDS scan is represented by the yellow arrow. Dotted lines in (e) and (f) demarcate the amorphous region.

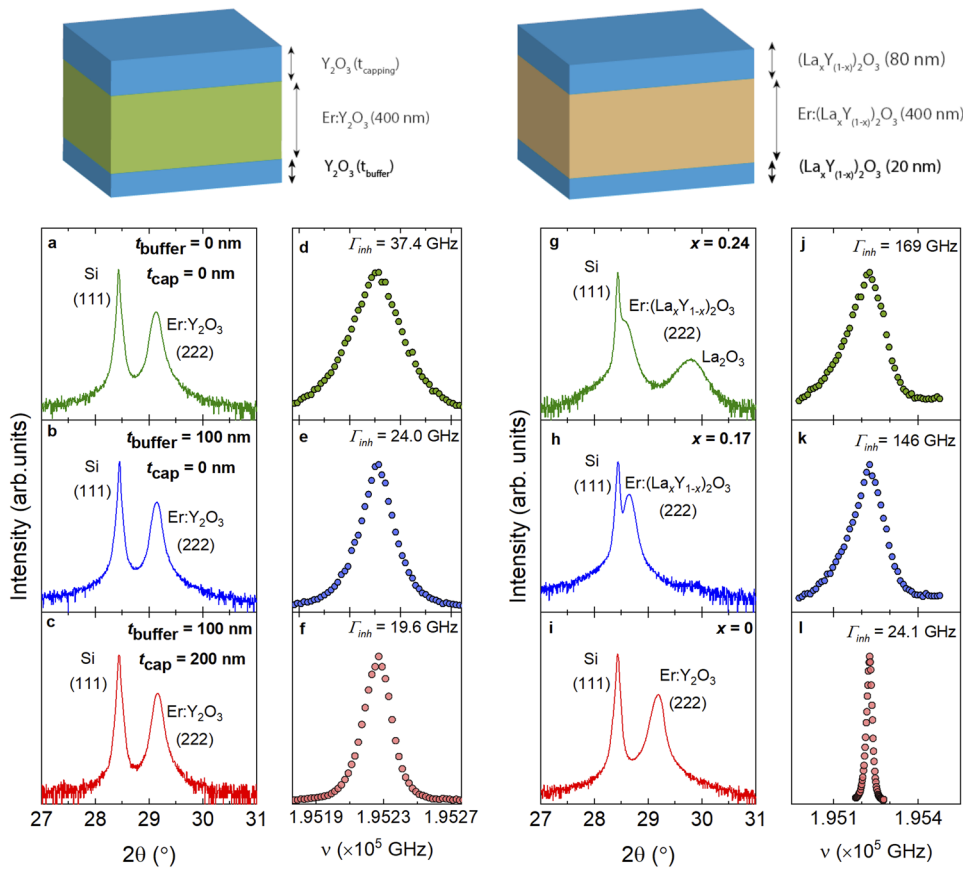


FIG. 4. The schematic at the top left represents the structure $(Y_2O_3)/(Er:Y_2O_3)/(Y_2O_3)$ used to probe the effect of the interface. [(a)–(c)] The XRD curve for the three films suggest similar crystal quality. (d) The baseline linewidth with no cap or buffer layer gives a Γ_{inh} of 37.4 GHz. (e) The addition of a bottom undoped layer improves this to 24.0 GHz. (f) Further adding a top undoped layer improves the linewidth to 19.6 GHz, giving an improvement of almost 50% over the baseline. On the top right, the schematic represents the structure $(20\text{ nm } Y_2O_3)/(400\text{ nm } Er:(La_xY_{1-x})_2O_3)/(80\text{ nm } Y_2O_3)$ used to study the effect of the La alloying of Y_2O_3 . The improvement in the lattice match is clearly indicated by the shift in the film XRD peak to Si [(g)–(i)]. However, the inhomogeneous optical linewidth also broadens as more La is added [(j)–(l)].

C. Spectroscopic characterization

The presence of Er^{3+} and its incorporation into the crystal structure were supported by EPR measurements and confirmed through the PL data. Figure 5(b) shows the EPR spectra for a 650 nm $Er:Y_2O_3$ film at 4.2 K (Er concentration ~ 10 ppm). Naturally occurring Er has multiple isotopes— ^{166}Er , ^{167}Er , ^{168}Er , and ^{170}Er —which constitute 33.50%, 22.87%, 26.98%, and 14.91% of naturally occurring erbium, respectively. ^{167}Er is the only isotope

with non-zero nuclear spin ($spin = 7/2$). The contribution from ^{167}Er is seen as eight smaller peaks in Fig. 5(b) distributed around the main peak at 548.24 ± 0.2 G that comes from the zero nuclear spin isotopes. A schematic is shown in Fig. 5(a). The relative intensities of these peaks are indicative of the abundance of different isotopes. The g -factor calculated for the central peak from the data shown in Fig. 5(b) is 12.2 and is attributed to be a composite of the contributions coming from the Er^{3+} ion at the C_2 sites.⁴⁴

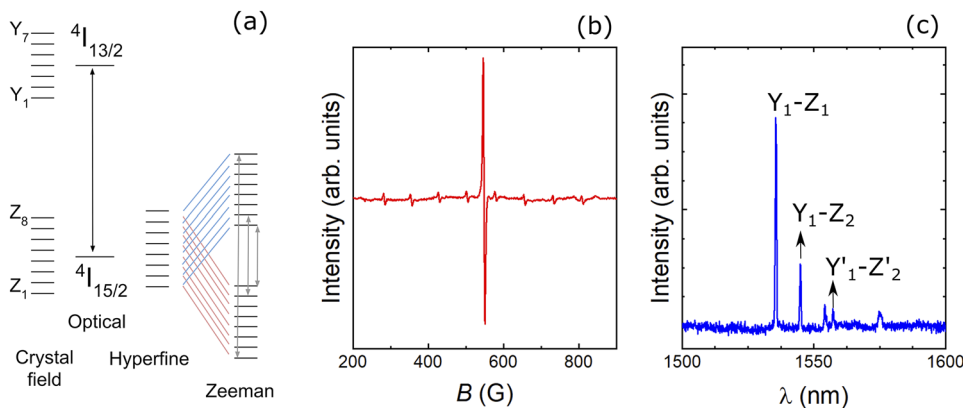


FIG. 5. (a) A schematic of the energy levels of interest in the Er^{3+} Stark levels from the crystal field effect (emission spectra) and the Zeeman splitting of the hyperfine levels which is seen in EPR. (b) EPR spectra show a large central peak from the zero nuclear spin isotopes of Er. Eight smaller peaks from the hyperfine transitions contributed by ^{167}Er are also seen. (c) Photoluminescence spectra from $Er:Y_2O_3$ films. Contribution from C_2 and C_{3i} sites is identified by the energies reported in the literature. This confirms the substitution of Er^{3+} for Y^{3+} in the bixbyite structure.

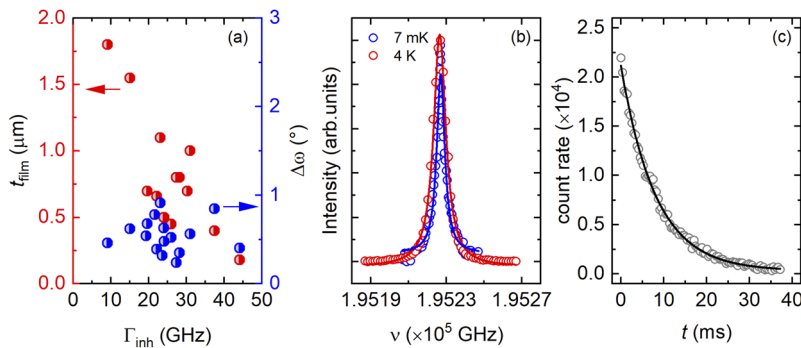


FIG. 6. (a) A strong linear correlation is seen between the PL linewidth and the film thickness (red); a comparison of the two metrics of disorder in the crystal quality, optical inhomogeneous linewidth (x-axis), and rocking curve FWHM (y-axis), however, shows no correlation (blue). (b) The narrowest linewidth obtained in our samples is 7.9 GHz at 4 K (red) and 5.1 GHz in the same sample in a dilution fridge setup (blue). (c) Optical excitation decay rate at the C_2 site was measured as 8.1 ms.

The crystal field effect breaks the spherical symmetry of the free ion, and this results in the splitting of the ground state ($^4I_{15/2}$) into 8 Stark levels and the first excited state ($^4I_{13/2}$) into 7 Stark levels—where the number of levels is dictated by the total angular momentum quantum number.¹³ Stark levels for the C_2 sites are represented as Z_i (Z_1 to Z_8) for the split $^4I_{15/2}$ levels and Y_i (Y_1 to Y_7) for the split $^4I_{13/2}$ levels, as shown in Fig. 5(a), and similarly as Y'_i and Z'_i for the C_{3i} sites. Figure 5(c) shows the PL data collected at 10 K in the wavelength range of 1500 nm–1600 nm. Emission peaks in this range is due to transitions between the Stark level manifold of the first excited state ($^4I_{13/2}$) and the ground state ($^4I_{15/2}$). Using the data reported in the literature,⁴⁵ the PL peaks at 1535.6 ± 0.01 nm, 1544.9 ± 0.04 nm, 1554.2 ± 0.1 , and 1575.1 ± 0.3 nm can be identified as the $Y_1 \rightarrow Z_1$, $Y_1 \rightarrow Z_2$, $Y_1 \rightarrow Z_3$, and $Y_1 \rightarrow Z_5$ transition, respectively, at the C_2 site. The peak at 1557.3 ± 0.3 nm is identified as coming from the $Y'_1 \rightarrow Z'_2$ transition at the C_{3i} site. This indicates that Er^{3+} is substituting for Y^{3+} in the crystal lattice.

Figure 6(a) shows the x-ray rocking curve full width at half maxima ($\Delta\omega$) (indicative of crystalline quality) and the film thickness as a function of the photoluminescence linewidth, Γ_{inh} . Films shown here have a bottom buffer and top cap in the range of 0–200 nm. Some of the films reported in Fig. 6(a) were grown specifically to check the thickness effect. The 1.8 μm film was unique in having a bottom buffer of $\sim 1 \mu\text{m}$. The erbium concentration for all these films is ≤ 200 ppm. The data show no clear correlation between the crystalline quality of the film and Γ_{inh} . This suggests that the optical properties of Er^{3+} in the Y_2O_3 host might not be limited by variations in lattice strain and the presence of growth defects such as dislocations in the host. This trend is unlike what is typically observed in band edge related emission in semiconductors, where poor crystal quality results in poor band edge photoluminescence. On the other hand, the plot of film thickness vs Γ_{inh} shows a strong inverse trend—thicker layers result in narrower photoluminescence linewidths. We attribute this to isolation of an increasing proportion of the active Er^{3+} from the top and bottom interfaces, which may result in impurity diffusion, as discussed earlier in this paper. Our best PL linewidth for C_2 site emission was found to be 7.9 GHz at 4 K and 5.1 GHz at 7 mK (base plate temperature on which the sample is mounted), as shown in Fig. 6(b). We estimate the actual sample temperature from laser heating to be <100 mK (supplementary material). The two measurements of the linewidths were carried out in two different measurement setups in order to gain more confidence in the data. The small

difference in linewidths in our view is most likely due to laser frequency calibration between the two setups and is not significant enough to suggest a temperature dependence of linewidth. In comparison with our thin film results, an inhomogeneous linewidth of 0.42 GHz and 2 GHz have been reported^{15,20} in bulk $Er:Y_2O_3$ polycrystalline (ceramic) and bulk single crystal systems. The optical excitation state decay measured for the PL in our samples was found to be 8.1 ms [shown in Fig. 6(c)], which is comparable to the reported value of 8.5 ms in the bulk single crystal²⁰ and $\sim 6\times$ longer than the lifetime of 1.5 ms reported for $Er:Y_2O_3$ atomic layer deposition (ALD) grown thin films.¹⁰ Why are the thin film linewidths broader than those reported in bulk films? In addition to the diffusion of impurities such as hydroxyl ions and silicon from neighboring interfaces, an important factor may be the effect of oxygen vacancies in subsurface regions—these are known as charge defects in many ionic oxides.

IV. CONCLUSION

The rare earth ion, Er^{3+} , offers attractive properties suitable for use as a quantum memory: a spin-optical interface, narrow photoluminescence linewidth, low spectral diffusion, and an emission wavelength in the telecom band. This paired with Y_2O_3 's low absorption in that wavelength range and epitaxial compatibility with Si makes $Er:Y_2O_3$ thin films on Si a promising material platform for quantum technologies. We have successfully demonstrated the growth of $Er:Y_2O_3$ epitaxial thin films on Si(111) and using spectroscopic techniques demonstrated the erbium substitutes for yttrium in the bixbyite structure at both the C_2 and C_{3i} sites where the optical decay lifetime obtained for the C_2 sites is comparable to that of bulk single crystals. We have further carried out a detailed microstructural and optical study of these epitaxial films. We have shown how bottom and top spacer (or buffer) layers can improve the Er photoluminescence linewidths in thin films. We show, importantly, that unlike band-edge-related photoluminescence in semiconductors, the photoluminescence of the Er^{3+} emission (Γ_{inh}) is unaffected by crystal quality, as determined by x-ray rocking curve linewidths. However, we show that the photoluminescence linewidths are directly correlated with film thickness, indicating surface and interface effects and potential impurity effects related to surfaces/interfaces. Lattice engineering using La leads to improvement in the mismatch with silicon but degrades Γ_{inh} significantly. Finally, we show that by optimizing the epitaxial growth conditions, we can obtain ultra-narrow

linewidths of 5.1 GHz in a dilution fridge setup (<100 mK) indicative of high quality Er^{3+} incorporation in a largely non-interacting host. Our next step would be measurement of coherence times on this thin-film system and comparison to values observed in the bulk.

SUPPLEMENTARY MATERIAL

See the [supplementary material](#) for details on the dilution fridge setup, further characterization, and lattice match calculations for the lanthanum alloyed films.

ACKNOWLEDGMENTS

This work was supported in part by the Center for Novel Pathways to Quantum Coherence in Materials, an Energy Frontier Research Center funded by the U.S. Department of Energy, Office of Science, Basic Energy Sciences, under Award No. DE-AC02-05CH11231. A.P., T.R., and T.Z. acknowledge the support from the Argonne National Laboratory's Laboratory Directed Research and Development (LDRD) program. Use of the Center for Nanoscale Materials, an Office of Science User Facility, was supported by the U.S. Department of Energy, Office of Science, Office of Basic Energy Sciences, under Contract No. DE-AC02-06CH11357. S.G. acknowledges the Vannevar Bush Fellowship under the program sponsored by the Office of the Undersecretary of Defense for Research and Engineering [OUSD (R&E)] and the Office of Naval Research as the executive manager for the grant.

DATA AVAILABILITY

The data that support the findings of this study are available from the corresponding author upon reasonable request.

REFERENCES

- H. J. Kimble, "The quantum internet," *Nature* **453**, 1023–1030 (2008).
- A. I. Lvovsky, B. C. Sanders, and W. Tittel, "Optical quantum memory," *Nat. Photonics* **3**, 706 (2009).
- W. Tittel *et al.*, "Photon-echo quantum memory in solid state systems," *Laser Photonics Rev.* **4**, 244–267 (2010).
- D. M. Toyli, C. D. Weis, G. D. Fuchs, T. Schenkel, and D. D. Awschalom, "Chip-scale nanofabrication of single spins and spin arrays in diamond," *Nano Lett.* **10**, 3168–3172 (2010).
- G. Wolfowicz *et al.*, "Optical charge state control of spin defects in 4H-SiC," *Nat. Commun.* **8**, 1876 (2017).
- A. M. Dibos, M. Raha, C. M. Phenicie, and J. D. Thompson, "Atomic source of single photons in the telecom band," *Phys. Rev. Lett.* **120**, 243601 (2018).
- P. Goldner, A. Ferrier, and O. Guillot-Noël, "Rare earth-doped crystals for quantum information processing," *Handb. Phys. Chem. Rare Earths* **46**, 1–78 (2015).
- T. Zhong *et al.*, "Nanophotonic rare-earth quantum memory with optically controlled retrieval," *Science* **357**, 1392–1395 (2017).
- D. D. Awschalom, R. Hanson, J. Wrachtrup, and B. B. Zhou, "Quantum technologies with optically interfaced solid-state spins," *Nat. Photonics* **12**, 516–527 (2018).
- M. Scarafagio *et al.*, "Ultrathin Eu- and Er-doped Y_2O_3 films with optimized optical properties for quantum technologies," *J. Phys. Chem. C* **123**, 13354–13364 (2019).
- J. G. Bartholomew *et al.*, "Miniaturizing rare-earth ion microwave to optical transducers," in *2018 Conference on Lasers and Electro-Optics (CLEO)* (Optical Society of America, 2018), pp. 1–2.
- G. P. Flinn *et al.*, "Anomalous optical dephasing in crystalline Y_2O_3 : Eu^{3+} ," *J. Lumin.* **58**, 374–379 (1994).
- G. Liu and B. Jacquier, *Spectroscopic Properties of Rare Earths in Optical Materials* (Springer, 2005).
- A. Perrot *et al.*, "Narrow optical homogeneous linewidths in rare earth doped nanocrystals," *Phys. Rev. Lett.* **111**, 203601 (2013).
- H. Zhang *et al.*, "Transparent Er^{3+} -doped Y_2O_3 ceramics with long optical coherence lifetime," *ACS Omega* **2**, 3739–3744 (2017).
- J. G. Bartholomew, K. de Oliveira Lima, A. Ferrier, and P. Goldner, "Optical line width broadening mechanisms at the 10 kHz level in $\text{Eu}^{3+}:\text{Y}_2\text{O}_3$ nanoparticles," *Nano Lett.* **17**, 778–787 (2017).
- N. Kunkel, J. G. Bartholomew, L. Binet, A. Ikesue, and P. Goldner, "High-resolution optical line width measurements as a material characterization tool," *J. Phys. Chem. C* **120**, 13725–13731 (2016).
- S. Elliott, M. Fanciulli, and G. Scarel, *Rare Earth Oxide Thin Films* (Springer Berlin Heidelberg, 2006), Vol. 106.
- D. Serrano, J. Karlsson, A. Fossati, A. Ferrier, and P. Goldner, "All-optical control of long-lived nuclear spins in rare-earth doped nanoparticles," *Nat. Commun.* **9**, 2127 (2018).
- C. W. Thiel, T. Böttger, and R. L. Cone, "Rare-earth-doped materials for applications in quantum information storage and signal processing," *J. Lumin.* **131**, 353–361 (2011).
- N. Kunkel and P. Goldner, "Recent advances in rare earth doped inorganic crystalline materials for quantum information processing," *Z. Anorg. Allg. Chem.* **644**, 66 (2018).
- T. Zhong and G. Philippe, "Emerging rare-earth doped material platforms for quantum nanophotonics," *Nanophotonics* **8**, 2003 (2019).
- T. Böttger, C. W. Thiel, R. L. Cone, Y. Sun, and A. Faraon, "Optical spectroscopy and decoherence studies of $\text{Yb}^{3+}:\text{YAG}$ at 968 nm," *Phys. Rev. B* **94**, 045134 (2016).
- E. Z. C. Afzelius, A. Tiranov, J. Lavoie, A. Ferrier, P. Goldner, N. Gisin, and M. Afzelius, "Efficient optical pumping using hyperfine levels in $^{145}\text{Nd}^{3+}:\text{Y}_2\text{SiO}_5$ and its application to optical storage," *New J. Phys.* **20**, 053013 (2018).
- J. M. Kindem *et al.*, "Characterization of $^{171}\text{Yb}^{3+}:\text{YVO}_4$ for photonic quantum technologies," *Phys. Rev. B* **98**, 024404 (2018).
- M. Rančić, M. P. Hedges, R. L. Ahlefeldt, and M. J. Sellars, "Coherence time of over a second in a telecom-compatible quantum memory storage material," *Nat. Phys.* **14**, 50 (2017).
- M. Zhong *et al.*, "Optically addressable nuclear spins in a solid with a six-hour coherence time," *Nature* **517**, 177 (2015).
- T. Zhong, J. M. Kindem, E. Miyazono, and A. Faraon, "Nanophotonic coherent light-matter interfaces based on rare-earth-doped crystals," *Nat. Commun.* **6**, 8206 (2015).
- S. Guha, N. A. Bojarczuk, and V. Narayanan, "Lattice-matched, epitaxial, silicon-insulating lanthanum yttrium oxide heterostructures," *Appl. Phys. Lett.* **80**, 766–768 (2002).
- C. W. Nieh *et al.*, "Nanometer thick single crystal Y_2O_3 films epitaxially grown on Si (111) with structures approaching perfection," *Appl. Phys. Lett.* **92**, 061914 (2008).
- S. C. Choi *et al.*, "Epitaxial growth of Y_2O_3 films on Si(100) without an interfacial oxide layer," *Appl. Phys. Lett.* **71**, 903–905 (1997).
- M.-H. Cho *et al.*, "Structural characteristics of Y_2O_3 films grown on oxidized Si(111) surface," *J. Appl. Phys.* **89**, 1647–1652 (2001).
- Materials Preparation Center, Ames Laboratory, U.S. DOE Basic Energy Sciences, Ames, IA, USA.
- M. McCormack, P. R. Platt, and R. K. Saxer, "Vapor pressure of dysprosium and erbium," *J. Chem. Eng. Data* **16**, 167–170 (1971).
- L. Pauling and M. D. Shappell, "The crystal structure of bixbyite and the c-modification of the sesquioxides," *Z. Kristallogr.* **75**, 128–142 (1930).
- J. Rosenthal and L. Yarmus, " $\text{SrO}:\text{Mn}$ as EPR marker and intensity standard," *Rev. Sci. Instrum.* **37**, 381 (1966).

- ³⁷A. Y. Bresgunov, A. A. Dubinsky, O. G. Poluektov, G. A. Vorob'eva, and Y. S. Lebedev, "Electron paramagnetic resonance of coals. New approaches to an old problem with multifrequency electron paramagnetic resonance and spin echo," *J. Chem. Soc., Faraday Trans.* **86**, 3185–3189 (1990).
- ³⁸S. Guha and V. Narayanan, "Oxygen vacancies in high dielectric constant oxide-semiconductor films," *Phys. Rev. Lett.* **98**, 196101 (2007).
- ³⁹V. Narayanan *et al.*, "Interfacial oxide formation and oxygen diffusion in rare earth oxide–silicon epitaxial heterostructures," *Appl. Phys. Lett.* **81**, 4183–4185 (2002).
- ⁴⁰S. Zafar, A. Callegari, V. Narayanan, and S. Guha, "Impact of moisture on charge trapping and flatband voltage in Al_2O_3 gate dielectric films," *Appl. Phys. Lett.* **81**, 2608–2610 (2002).
- ⁴¹H. J. Osten *et al.*, "Molecular beam epitaxy of rare-earth oxides," in *Rare Earth Oxide Thin Films* (Springer, 2006), pp. 101–114.
- ⁴²B. M. Tissue, N. J. Cockcroft, L. Lu, D. C. Nguyen, and W. M. Yen, "Comparison of the spectra and dynamics of $\text{Er}^{3+}:\text{Y}_{2-x}\text{Sc}_x\text{O}_3$ ($x = 0, 1, 2$)," *J. Lumin.* **48-49**, 477–480 (1991).
- ⁴³K. W. Jang and R. S. Meltzer, "Homogeneous and inhomogeneous linewidths of Eu^{3+} in disordered crystalline systems," *Phys. Rev. B* **52**, 6431–6439 (1995).
- ⁴⁴G. Reinemer, "Optical characterization of perturbed sites and C_{3i} sites in rare earth doped oxide crystals," Ph.D. thesis, Montana State University, 2003. Power saturation behavior on polycrystalline ($\text{Er}:\text{Y}_2\text{O}_3$) samples performed in our lab also helped us identify this peak as coming from C_2 sites.
- ⁴⁵J. B. Gruber *et al.*, "Modeling optical transitions of $\text{Er}^{3+}(4f^{11})$ in C_2 and C_{3i} sites in polycrystalline Y_2O_3 ," *J. Appl. Phys.* **104**, 023101 (2008).